Implementation of an elastic no-tension material model in a sequentially linear analysis framework

Grigor Angjeliu, Matteo Bruggi, Alberto Taliercio

Department of Civil and Environmental Engineering, Politecnico di Milano

Abstract

Sequential Linear Analysis (SLA) has been recognized by researchers as a valid alternative for the analysis of brittle materials compared to incremental-iterative finite element solutions. The elastic no-tension masonry-like material model, with infinite strength in compression and negligible tensile strength, has been implemented in plane stress conditions within the SLA framework.

The isotropic no-tension masonry-like material is replaced with an orthotropic one, which exhibits a negligible response along material axis where the principal stress reads positive. In the SLA framework, a series of linear elastic analyses are carried out, sequentially aligning material axes with principal stress directions, and reducing directional stiffness at the critical material points where positive stresses are found. This process is carried out up to the point when the change in the total strain energy finds a plateau. The implementation follows a combined application of a user subroutine in Abaqus with Matlab and Python scripts.

Several cases dealing with self-weight, settlements and horizontal loading are developed to demonstrate its applicability. The results demonstrate the possibility to generate compressive stress fields, with tensile stresses virtually vanishing at all material points.

1 Introduction

Masonry-like materials are unable to withstand (significant) tensile stresses. From a mechanical point of view, this means that the stress field is semi-definite negative all over the body. Two subclasses of no-tension (NT) material models have been developed in the literature: (i) the Rigid No-Tension (RNT) and (ii) Elastic No-Tension (ENT) model.

The simplest version is the RNT material model, which is a unilateral model that assumes the material to be infinitely stiff in compression, but unable to carry tensile stresses [1]. This model was firstly introduced within the framework of the theory of plasticity by Heyman [2], and then further developed to be implemented in computer programs for practical applications based on energy minimisation principle [3-5], or accounting for large displacements [6]. The RNT model requires no material properties, and the results are exclusively depending on loads and geometry. A number of authors have applied this material model to compute the limit load of masonry walls, arches and vaults [2, 7, 8], or to investigate the effect of ground settlements [9, 10].

A second subcategory of NT materials corresponds to the ENT model, which considers finite stiffness in compression [1, 11]. This model to compute the limit load of masonry-like structures, as well as for the analysis under service loads. Strains can be positive or negative: positive strains are fully inelastic, whereas negative strains correspond to elastic, compressive deformation. Therefore, the model requires only the modulus of elasticity (in compression) as input parameter.

In the last decades a number of refined models have been developed for masonry structures based on the theory of plasticity and damage mechanics [12, 13]. Although they have been shown to be quite accurate in simulating the mechanical behaviour of masonry specimens or small-scale buildings tested in the laboratory, they require many parameters which are usually unavailable for practical applications. On the other hand, NT material models are very attractive, since they require no or few parameters. A comparison between limit analysis solutions and finite element methods for the stability assessment of masonry structures is addressed in [9, 14].

Despite the apparent simplicity of the linear ENT model, the need to treat discontinuities in the stress and displacement fields gives rise to several numerical problems, which results in many convergence issues [7]. In fact, application of NT material models remains still limited. Readers are referred to Angelillo [15, 16], who proposed a FE solution based on a complementary energy theorem for ENT bodies, or to Bruggi and Taliercio [17, 18] who reformulated the analysis of 2D and 3D NT structures as a topology optimization problem.

The present work fits into the path of the latter contributions [17-19]. The solution of the inherent non-linear problem is tackled herein by resorting to the concept of Sequential Linear Analysis (SLA), instead of implementing the energy-based procedure that were originally proposed to this goal. SLA was developed as a robust alternative to incremental-iterative finite element solutions for brittle materials [20, 21], and is herein extended in this study to ENT masonry-like material. In the present version, the approach is limited to 2D bodies, with some generalization to 3D structures. The procedure is a step-by-step approach, considering a series of linear elastic analyses with updated mechanical parameters from the previous analysis. The original isotropic material is replaced by an orthotropic one, which exhibits a negligible response along any material axis when the principal stress tends to become positive. The process of updating material axis orientation and reducing the local stiffness continues sequentially until convergence is achieved.

The paper is organized as follows. Section 2 describes the methodological framework, the governing equations of the NT material model, the SLA procedure, and the algorithm of the current implementation. Sections 3 focuses on several applications demonstrating the capabilities of the ENT model in the case of structures subjected to gravity loads, horizontal loads, and soil settlements. The results show the possibility to generate compression stress field with vanishing tensile stresses. Furthermore, the computations yield good prediction of the limit load compared to analytical and experimental benchmarks. Finally, the main results are critically discussed in section 4, and the main conclusions are summarized.

2 Methodology

2.1 Governing equations for ENT material

Details on the ENT material model can be found in a number of papers (see e.g., [1, 11, 22]). Hereafter, the governing equations of the ENT model are only briefly recalled. The mechanical constraints that a linear ENT material must fulfil can be described mathematically as follows. The stress tensor must be negative semidefinite:

$$\sigma_{ij} \in Sym^{-},$$

where Sym^{-} is the closed cone of the negative semi-definite symmetric second order tensors.

The strain tensor is assumed to consist of two parts: an elastic part ε_{ij}^{e} and an inelastic (latent) part ε_{ij}^{c} accounting for cracking:

$$\varepsilon_{ij} = \varepsilon_{ij}^{e} + \varepsilon_{ij}^{c}.$$

Finally, the elastic strain is related to the stress σ_{hk} through the generalized Hooke's law defined by the elasticity tensor C_{ijhk}, while the latent part of the strain, ε_{ij}^{c}, follows the normality condition:

$$\sigma_{ij}\varepsilon_{ij}^{c} = 0, \quad \text{and} \quad \varepsilon_{ij}^{c} \in Sym^{+},$$

where Sym^{+} is the closed cone of the positive semi-definite symmetric second order tensors.

2.2 Material model

An isotropic Elastic No-Tension ENT masonry-like material has no strength in tension and infinite strength in compression. Therefore, it requires only two mechanical parameters: a) modulus of elasticity E_0, and b) Poisson's ratio ν_0. In the uniaxial case, the stress-strain law is illustrated in Fig. 1. Negative strains correspond to elastic compressive deformations, while positive strains correspond to cracking strains. The inherent non-linearity is implemented as a series of stiffness reductions, following the violation of a stress criterion at each integration point, until a negligible stiffness E_n is attained (Fig. 1).

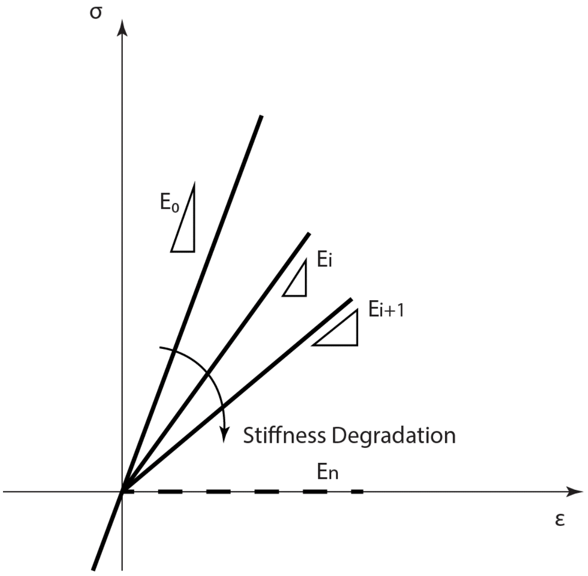

Fig. 1. Uniaxial law for linear elastic no-tension material.

In the 2D case, under plane stress conditions, the isotropic material is replaced by an equivalent orthotropic one, with a vanishing stiffness along any principal tensile stress direction. A 4-node plane stress element with one integration point is used in Abaqus simulations (Fig. 2a). The symmetry axes $\tilde{z}_1$, and $\tilde{z}_2$ of the equivalent orthotropic material and the principal stress directions z_I, and z_{II} of the no-tension solid share the same orientation with respect to the general reference system Oz_1z_2 (Fig. 2b). This is achieved through a process of alignment of the symmetry axes of the equivalent orthotropic material with the principal stress directions, $\tilde{z}_\alpha$, α=I, II, detected in the no-tension medium.

The principal stresses are computed as the eigenvalues of the stress tensor at the Gauss points, whereas the principal directions are found as the relevant eigenvectors. In the plane stress case, the principal stresses are related to the Cartesian stresses by:

$$\sigma_{I,II} = \frac{\sigma_{11} + \sigma_{22}}{2} \pm \sqrt{\left(\frac{\sigma_{11} - \sigma_{22}}{2}\right)^2 + \sigma_{12}^2}$$

whereas the orientation of the principal stress direction $\tilde{z}_I$ is rotated with respect to the axis z_1 of the global reference system of an angle:

$$\theta = \frac{1}{2}\tan^{-1}\left(\frac{2\sigma_{12}}{\sigma_{11} - \sigma_{22}}\right).$$

The matrix that transforms the 2D principal stresses into Cartesian stresses reads:

$$\mathbf{T} = \begin{bmatrix} cos^2\theta & sin^2\theta & -2\, cos\,\theta\, sin\,\theta \\ sin^2\theta & cos^2\theta & 2\, cos\,\theta\, sin\,\theta \\ cos\,\theta\, sin\,\theta & -cos\,\theta\, sin\,\theta & cos^2\theta - sin^2\theta \end{bmatrix}.$$

In order to track cracking strains, at each Gauss point, two nondimensional material densities $\rho_i \in (0,1]$, $i = 1,2$, are introduced along the material symmetry axes $\tilde{z}_1$ and $\tilde{z}_2$. The material densities ρ_i govern the stiffness penalization of the orthotropic material and are related to the damage variables D_i, $i = 1,2$, though the expression $D_i = (1 - \rho_i)$. If one of the principal stresses becomes positive, the material density variable is initialized with a nonzero value, $\rho_0 = 0.1$, while further reductions are performed using a quadratic reduction factor:

$$\rho_{k+1,i} = 1 - \left(1 - \rho_{k,i}\right)^2, i = 1,2.$$

Similar criteria are also proposed in the literature in [23] [24]. In this process, the initial elastic modulus, E_0, is penalized in the i-th principal stress direction by the nondimensional material density $\rho_i \in (0,1]$. In each direction, the model can capture negative, elastic compressive strains, or positive strains which correspond to cracking strains. In the latter case a scaled stiffness is computed in the direction where the principal stress would become positive, in order to account for cracking. Hence, the updated values of the Young's moduli, $\tilde{E}_1$, $\tilde{E}_2$ and the shear modulus are reduced at each Gauss point when the criteria is violated:

$$\tilde{E}_1 = \rho_1 E_0, \qquad \tilde{E}_2 = \rho_2 E_0, \qquad \tilde{G}_{12} = \rho_1\rho_2 \frac{E_0}{2(1+\nu_0)}$$

At the same time also the initial Poisson's ratio ν_0 is updated by means of the same factors ρ_i:

$$\tilde{\nu}_{12} = \rho_1 \nu_0, \quad \tilde{\nu}_{21} = \rho_2 \nu_0$$

Transformation regarding the reduction of stiffness along the symmetry axes of the material are discussed by a number of authors [19, 25, 26]. The process and its stages are described in Fig. 2. In particular, the stress-strain law written in the material system of the equivalent orthotropic medium reads:

$$\boldsymbol{\sigma} = \boldsymbol{D}\,\boldsymbol{\varepsilon},$$

where the arrays that gather the 2D Cartesian stress and strain components are $\boldsymbol{\sigma} = [\sigma_{11} \ \ \sigma_{22} \ \ \sigma_{12}]^T$, $\boldsymbol{\varepsilon} = [\varepsilon_{11} \ \ \varepsilon_{22} \ \ 2\varepsilon_{12}]^T$ and:

$$\boldsymbol{D} = \boldsymbol{T}(\theta)\ \widetilde{\boldsymbol{D}}\ \boldsymbol{T}(\theta)^{\boldsymbol{T}}.$$

The stiffness matrix in the material (principal stress) reference system can be written as:

$$\widetilde{\boldsymbol{D}} = \frac{1}{1-\tilde{\nu}_{12}\tilde{\nu}_{21}}\begin{bmatrix} \tilde{E}_1 & \tilde{\nu}_{12}\tilde{E}_2 & 0 \\ \tilde{\nu}_{21}\tilde{E}_1 & \tilde{E}_2 & 0 \\ 0 & 0 & \tilde{G}_{12}(1-\tilde{\nu}_{12}\tilde{\nu}_{21}) \end{bmatrix},$$

where:

$\tilde{E}_1$, $\tilde{E}_2$ = the elastic moduli along the equivalent material axis $\tilde{z}_1$, $\tilde{z}_2$.

$\tilde{G}_{12}$ = the in-plane shear modulus,

$\tilde{\nu}_{12}$, $\tilde{\nu}_{21}$ = the Poisson's ratios; the symmetry condition $\tilde{\nu}_{12}\tilde{E}_2 = \tilde{\nu}_{21}\tilde{E}_1$ holds.

It is noted here that the implemented approach resembles a smeared crack model, where discontinuities are captured in terms of strains in the continuum model. In a no-tension material, cracking strains represent all the crack opening since the material cannot elastically deform in tension, whereas in other types of materials it is the sum of crack opening and deformation of the material between the cracks [27].

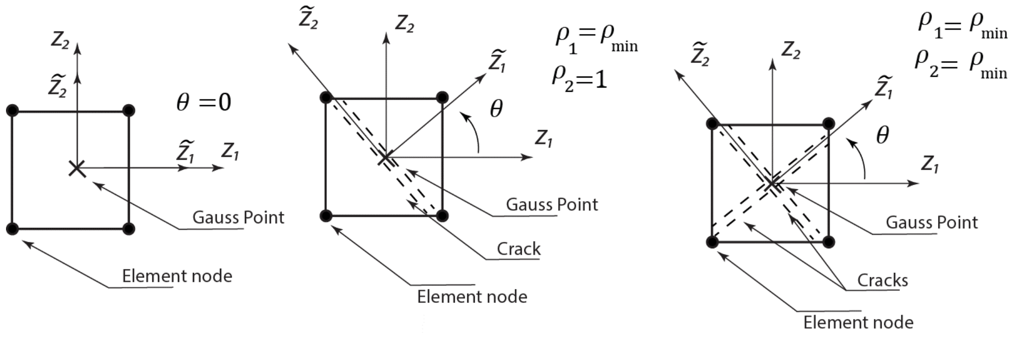

a) *b)* *c)*

Fig. 2. State of stress transition in a plane stress element: a) initial state, b) damage onset normal to positive principal stress, c) void phase with biaxial damage.

2.3 Implementation workflow

The implementation is based on a combined use of the Abaqus User Field Subroutine USDFLD, the Abaqus User-Subroutine-defined initial solution-dependent state variable fields SDVINI, Python and Matlab scripts. The Matlab script is the central element of this process, which updates the Abaqus input files and launches the Abaqus analysis.

The User Field Subroutine, USDFLD, is used to define field variables ρ_i at the integration points as functions of any of the stresses, σ_{11} and σ_{22}, which coincide with the principal stresses. In each analysis, for each of the finite elements, the vector $(\rho_i\,, \theta)$ is given, where $i = 1, 2$ defines the damage direction. The material density parameters can vary in the range $\rho_{min} \leq \rho_i \leq 1$. The minimum value ρ_{min} is a strictly positive value, so as to avoid numerical instability.

The second parameter is the rotation θ. Stresses are exported in Matlab through a Python script and are postprocessed to calculate the in-plane principal stress direction. The new rotations are updated in the orientation section of the input file before the subsequent analysis is launched.

The alignment of the symmetry axes of the fictitious orthotropic material w.r.t. the principal stress directions of the no-tension medium is achieved in a number of steps. The results show that usually convergence is achieved in 15 iterations. The change in orientation for each element (excluding the void elements) in the last step of the convergence of this alignment procedure is usually less than 0.1 degree. This could be used as a termination criterion. Alternatively, it was preferred to adopt a criterion based on the change in strain energy ψ, which reads:

$$\Delta\psi = \frac{\psi_{i+1} - \psi_i}{\psi_i} < \varepsilon$$

The value of ε is typically set to 10^{-3} of the current value of the energy.

In order to prevent singularities and excessive deformations, the elements with fully penalized stiffness in both directions are removed from the simulation. This is achieved with the element deletion technique. It is used for elements with biaxial damage (void phase with $\rho_1 = \rho_2 = \rho_{min}$). Deleted elements have no ability to carry stresses and, therefore, have no contribution to the stiffness of the model. A third state variable SDV3 is added as an element deletion flag.

The User subroutine SDVINI is used to initialize the solution-dependent state variable fields at each material point. The state variables controlling the damage computed in the previous analysis, SDV1, SDV2, are exported to a text file and imported afterwards in the new analysis, through the SDVINI subroutine.

This process is summarized though algorithm 1, Solve.

```
Algorithm: Solve
------------------------------------------------------------

INPUT:
        Youngs's Modulus $E_0$
        Poisson's ratio $\nu_0$
        Maximum number of iterations $Niter_{max}$
        Initial Strain Energy $\psi_1 = 0$
        Current step, $i = 1$

Run 1st Abaqus Elastic Analysis
Read Stress Values (via Python script)
Compute Principal Stresses
```

```
Update Material Axis Rotation
Create New Input file
Run Abaqus Analysis (with USFLD subroutine)
Read Strain Energy $\psi$

while $\Delta\psi > \varepsilon$ and $i < Niter_{max}$

    Read Stress Values (via Python script)
    Read State Variable SDV (via Python script)
    Compute Principal Stresses
    Update Material Axis Rotation
    Update Damage matrix
    Create New Input file
    Run i-th Abaqus analysis (with USFLD & SDVINI subroutine)
    Read Energy $\psi$
end while
------------------------------------------------------------
```

2.4 Collapse load tracking

The approximated collapse load is calculated using a procedure inspired by the bisection method. The central idea is that due to the monotonic trend of a pushover curve for a linear elastic no-tension structure, equilibrium is lost between a step successfully converged and a step that did not converge. A similar procedure was proposed previously by Bruggi and Taliercio in [18] using an energy-based solution for the ENT problem. The authors demonstrated that the collapse multipliers evaluated using the bisection method and a classical incremental approach are very similar. Typically, the horizontal shear force is plotted versus the displacement of a control point. The limit load is evaluated at the plateau of the curve, where small increments in load are matched by remarkable displacement increments, which prelude the loss of equilibrium of the system.

In the recent years, when dealing with the seismic performance definition of existing buildings beside the evaluation of the limit load, the evaluation of the displacement capacity has emerged as a crucial issue. A limit displacement may be conveniently related to failure of the material in compression. To this goal the displacement capacity is assumed to be attained when the applied load induces a compressive stress equal to the strength of the material in compression, f_c, in any finite element of the model. The criterion, although quite conservative, turns to be in line with the brittle nature of masonry (see section 3.1).

The collapse load is tracked with the algorithm 2, *Limit Load*. In principle, the algorithm monotonically increases a chosen load up to the activation of a collapse mechanism that causes loss of equilibrium in the system. Depending on the case study, the loads can be horizontal forces (simulating earthquake loads in a seismic analysis), gravity loads, vertical forces simulating vehicle load in the case of bridges, etc.

The procedure starts with the initialization of several variables as force increment ΔF, force tolerance F_{tol}, maximal number of steps N_{max}, and the limit load, F_0. The iterative search of the collapse load proceeds until the force increment, $\Delta F,$ is smaller than a predefined force tolerance, F_{tol}, or a stop criterion defined by a maximum number of iterations N_{max}.

At each iteration, convergence is searched for the load F_{trial}. At the beginning the trial load is increased from 0, with a standard predefined increment ΔF. The value ΔF is kept fixed if the procedure *Solve* converges. If it does not, at each iteration within a step, i, the value of ΔF is decreased. In this case, the trial force F_{trial} is defined by the bisection method, as the average of the previous successful trial load and the current unsuccessful trial load. At each converged step of the procedure *Solve*, the limit load and the monitored displacements are saved. Finally, the limit load, the displacement vector and the number of steps required to achieve the solution are printed.

Algorithm: *Limit Load*

```
----------------------------------------------------------
INPUT:
        Force increment $\Delta F$
        Force tolerance $F_{tol}$
        Max number of steps $N_{max}$
        Limit load, $F_0 = 0$
        Current step, $i = 1$

$F_{trial} = F_0 + \Delta F$

while $\Delta F > \Delta F_{tol}$ and j< $N_{max}$

Run Solve for $F_{trial}$

        If Solve converged then
                $F_i = F_{trial}$
                Save $u_i$
                $F_{trial} = F_0 + \Delta F$
                $i = i + 1$

                else
                $\Delta F$= $(F_{trail} - F_i)/2$
                $F_{trial} = F_{i-1} + \Delta F$
        end if
end while

print ($F_i$, $u_i$, $i$)

----------------------------------------------------------
```

3 Applications

A series of analyses with the ENT material were carried out, aiming at testing the applicability of the model to the study of unreinforced masonry walls. The main results are shown hereafter.

Two application categories are considered:

a) Lateral load capacity analysis, and

b) Settlement analysis.

Each analysis considers two steps. In the first load step, the self-weight and a possible vertical precompression (dead loads) are applied. The second step considers the application of the horizontal, live load, or prescribed vertical settlements.

In the case of the lateral loading analysis, the applied horizontal force and the displacement of the top corner node were monitored to obtain the force-displacement curve. In all the simulations the principal stresses are visualized and, in some cases, also the "void" elements (with $D1=D2\approx 1$). Both can be compared with the experimental crack pattern, if available. The comparison must be made with due care, as the model captures distributed cracking strains rather than discrete cracks.

3.1 Lateral load capacity analysis

3.1.1 Panel under vertical precompression and horizontal loading

A slender masonry panel with dimensions 2.7m x 1.1m x 0.102 m (Fig. 3a), similar to that tested at TU Delft in experiment TUDCOMP-20, is adopted to validate the proposed numerical procedure [28, 29]. The panel is loaded vertically with a precompression 0.63MPa. The pressure is applied through a horizontal steel beam mounted at the top of the wall and is kept constant for the entire duration of the experiment. Consequently, a cyclic horizontal displacement is applied at the steel beam through actuators. As reported in [28], the rocking response with heel tension and toe crushing were observed during the final stages. This is an expected response when testing slender panel under lateral loading.

The numerical model is shown in figure Fig. 3b. At the top, a row of elastic elements is inserted to consider the steel beam (white elements in Fig. 3b). The domain is discretised with square 100 mm x 100 mm elements. The top steel beam is allowed to rotate similarly to the experimental setup. The same test was considered previously also in [20], to test SLA procedures. The material properties are: E_0=4972 MPa, ν_0=0.16, f_c=6.35 MPa. The precompression is applied through a distributed load equal to 64.26 N/mm, which corresponds to a vertical stress of 0.63 MPa.

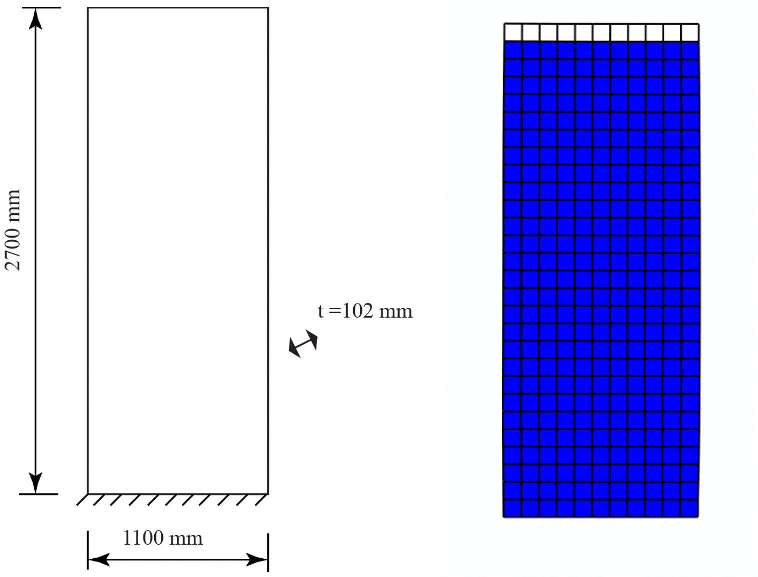

Fig. 3.a) TUDCOMP-20 test panel, b) Numerical model of the TUDCOMP-20 test.

The numerical model with the ENT material shows the tensile cracking since the early stages of the analysis. A compression diagonal strut occurs within the wall, which transmits the actuator force to the base (Fig. 4). As the load increases, the width of the lower part of the strut dramatically decreases, in conjunction with the development of heel tension and the increase in compressive stress at its tip. In Fig. 4 the distribution of the principal stresses and the void phase (in blue) at the final converged stage, corresponding to the numerically predicted collapse, are shown. At the toe, the compressive strength limit, 6.35 MPa, is attained.

The capacity curve is defined using the algorithm presented in section 2.4, by using an initial guess $\varDelta F = 5\ kN$ and a tolerance $F_{tol} = 0.02kN$. Convergence is achieved in 5 successful steps.

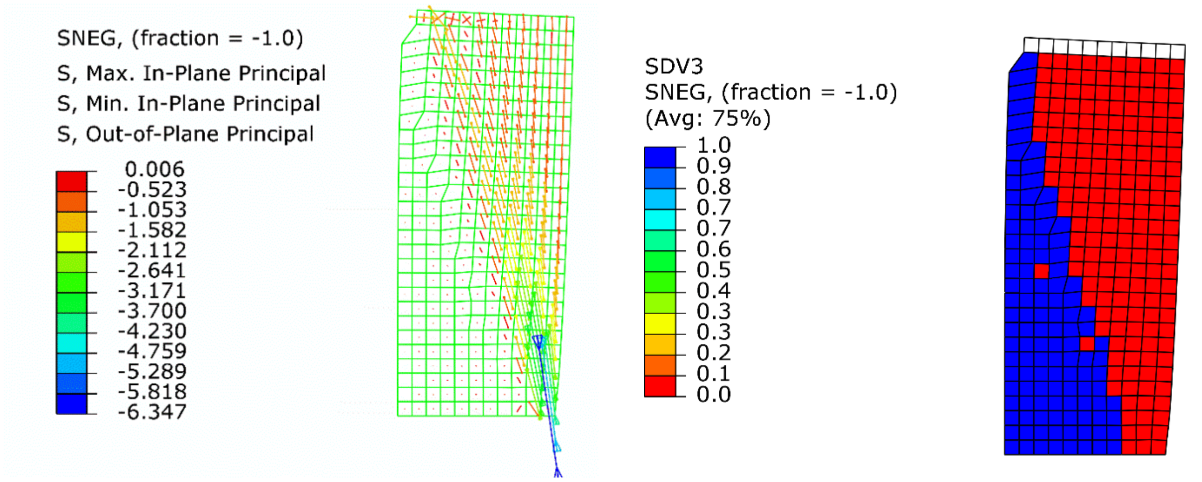

Fig. 4. TUDCOMP-20 test panel. Left: distribution of the principal stresses in the wall, at the final stage; right: distribution of the "void" elements, i.e. with biaxial damage (in blue).

The estimated collapse load is 12.77 kN and matches fairly well the sub-horizontal experimental branch, which occurs at about 12.4 – 12.8 kN.

A hand calculation of the collapse load of a simple panel overturning under vertical precompression and horizontal loads gives a value of 14.4 kN if the hinge is formed at the toe, or 13.1 kN if the hinge is at 50 mm from the wall edge. The second value is more representative of our case, as in the numerical model the hinge can activate at half the width of the toe finite element, that is, 50mm. Therefore, the numerical collapse load and the analytical value differ by 2.4%.

Regarding the displacement capacity, the limit analysis can predict only the limit load. Nevertheless, if considered a finite strength in compression, f_c=6.35 MPa, the predicted displacement in the last stable increment is 13.2 mm. The estimated drift is 0.49%, is in line with considerations on the normative EN 1998-3:2005 where the capacity of an unreinforced masonry wall controlled by shear expressed in terms of drift is equal to 0,4%. Compared to the experimental results, the value of the drift of 0,4% considered in the codes, is too conservative if referred to the values that can be observed in experimental tests that are often in the range 5-10% of the height.

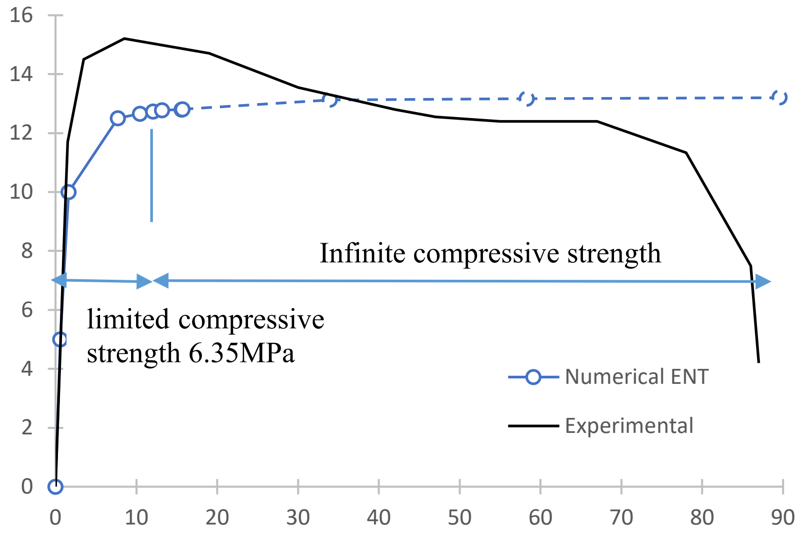

Fig. 5. TUDCOMP-20 test panel: comparison of the experimental [28] and numerical capacity curves.

3.1.2 Portal frame under vertical precompression and horizontal loading

The capacity of a masonry portal formed by two piers and a spandrel is considered in this section. The geometry of the model is reported in Fig. 6a. The portal is discretised with a mesh of 150 x 150 mm square elements (Fig. 6b). The wall thickness is 350mm. The material properties are: E_0=2500 MPa, ν_0=0.2. The strength in compression f_c is assumed to be infinite.

The system is loaded with a vertical pre-compression q=15kN/m and a horizontal force $F = \lambda p H_2$ that increases up to collapse. The top right corner is used as control point to monitor the lateral displacements. The horizontal, live load λp is applied along the top edge of the masonry pier, and its reference value is expressed as:

$$p = \frac{q(L_1 + L_2 + L_3)}{H_2} = \frac{q(1800 + 1200 + 1200)}{600} = 105kN/m$$

(see Fig. 6a). The solution obtained using the proposed ENT model will be compared with the analytical solution that was previously developed in [18], where the collapse multiplier was found to be 0.3545, and the corresponding limit load F=$\lambda p H_2$ =22.334kN.

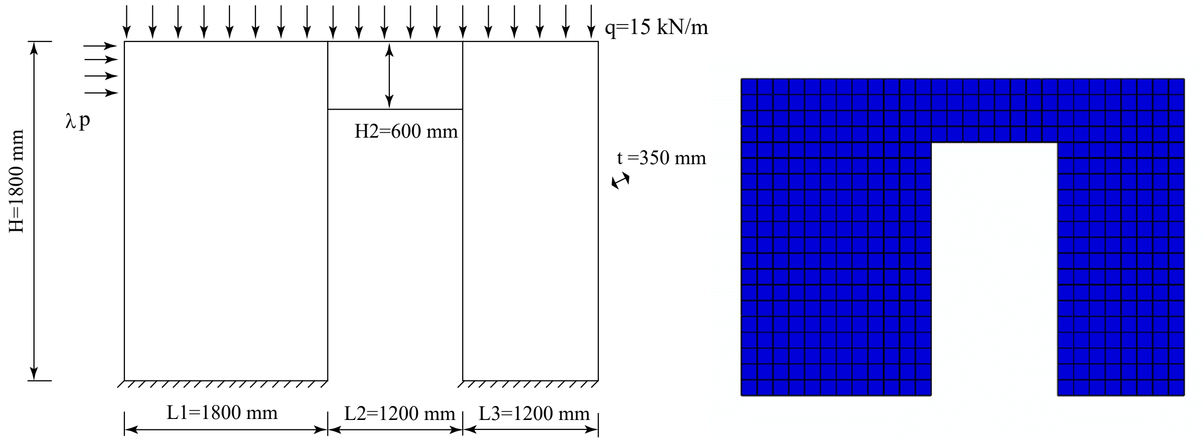

(a) (b)

Fig. 6. a) Geometry of the panel according to [18], b) Finite element mesh.

The first simulation with ENT material includes only vertical precompression. The simulation shows the formation of an arch-like mechanism (Fig. 7a). The central area of the spandrel behaves as a void phase, where both principal stresses are positive (blue elements in Fig. 7b). These elements are deactivated from the simulation using the element deletion technique of Abaqus. The compressive stresses in the strut in the right pier are slightly higher, because of its reduced dimensions compared to the left pier.

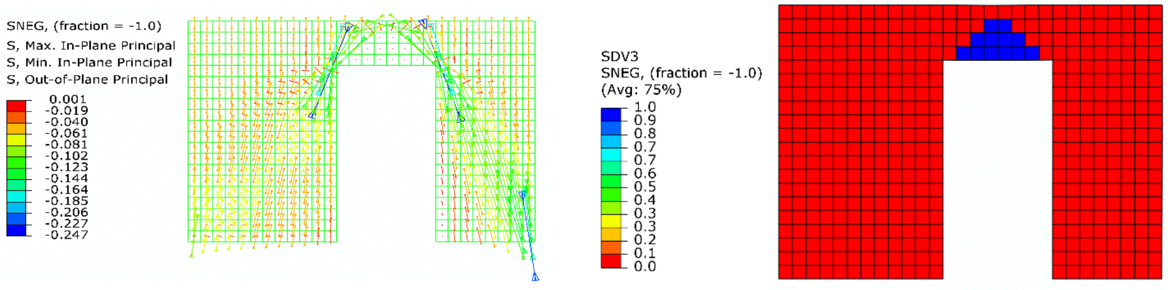

(a) (b)

Fig. 7. Distribution of principal stresses in masonry due to vertical precompression, b) "Void" elements, with biaxial damage (in blue).

Starting from the dead load only (Fig. 7), as the horizontal pressure increases different types of compression struts occur in each pier. The left strut changes from prismatic-shaped to fan-shaped, while the right pier strut maintains the bottle shape strut up to the end (Fig. 8). The distribution of the compression stresses at the base of each pier becomes triangular (Fig. 8), until complete hinges form at the onset of collapse. Collapse corresponds to a sort of sway mechanism, with hinges also atop the two piers (Fig. 8).

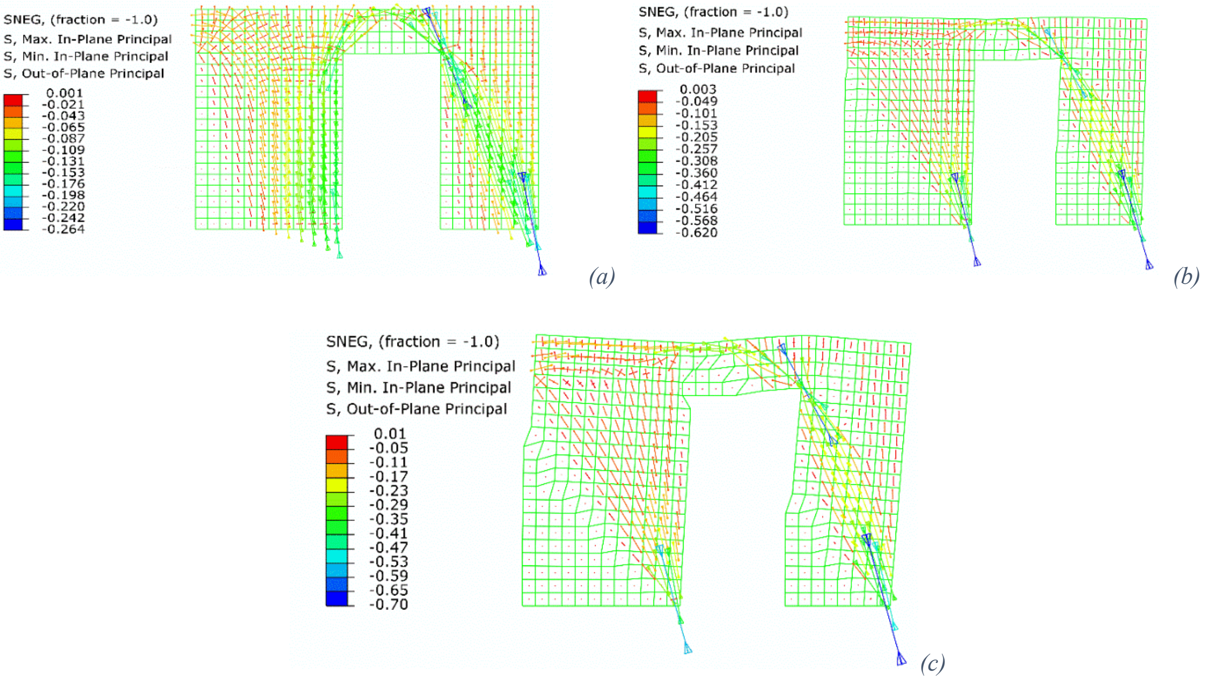

Fig. 8. Principal stresses at different values of the load multiplier: a) F=10 kN and λ=0.097, b) F=20 kN and λ=0.317, c) F=22.695 and λ=0.36.

The limit load is estimated using the algorithm presented in section 2.4, by using an initial guess, $\Delta F = 10\ kN$ and a tolerance, $\Delta F_{tol} = 0.04kN$ (Fig. 9).

Convergence is achieved in 11 iterations, with a total of only 5 converged steps. The computed limit load is F=22.695 kN, and the collapse multiplier λ=0.36. The difference with respect to the analytical value is only 1.62%.

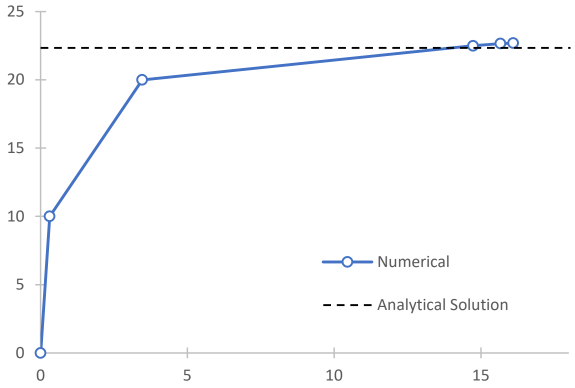

Fig. 9. Comparison of experimental and numerical shear vs displacement capacity curves.

3.1.3 Masonry façade under vertical precompression and horizontal loading: Pavia experiment

The “Pavia experiment” [30] is a well-known benchmark for masonry buildings under horizontal loading. A two-story masonry façade is tested under horizontal cyclic loading. The geometry of the building façade is reported in Fig. 10a. Beside the masonry self-weight, an additional gravity load is applied at each floor level, resulting in 248.4 kN for the first floor and 236.8 kN for the second floor. The reported crack pattern, which is related to cyclic loading is shown in Fig. 10b.

The façade is discretized by square, 230 mm-side elements, for a total of 616 linear plane stress quadrilateral elements with reduced integration, labelled CPS4R according to Abaqus nomenclature (Fig. 10c). Three other mesh discretization are addressed for a mesh sensitivity study, namely two structured mesh with 115 mm- and 300 mm- side elements, and an unstructured mesh with elements having average side equal to 230 mm. The lintels are assumed to behave elastically (white elements in Fig. 10c), as no cracking is expected here, while the ENT material is used elsewhere. In the numerical simulations, first the gravity load is applied and then kept constant; in a second step, a horizontal load is applied and monotonically increased until collapse is attained (as described in section 2.4).

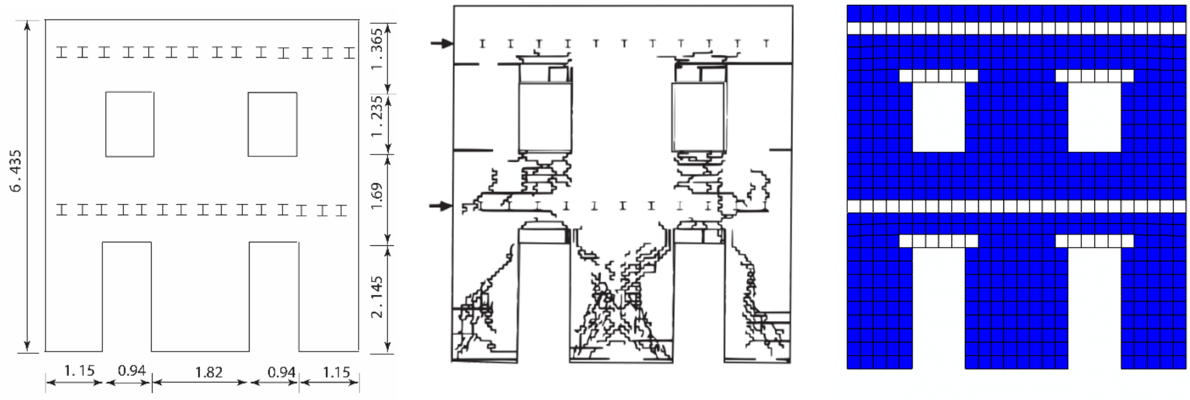

Fig. 10. Façade of the “Pavia building” [25]: a) Geometry, b) Experimental damage pattern, c) Numerical model discretization.

Considering the mesh with 230 mm-side elements, an average compressive stresses of 0.4 – 0.5 MPa is computed under gravity load (Fig. 11), similarly to what reported in [30]. Slightly higher values are computed locally close to lintels. However, no important cracking is found in the spandrels due to the presence of elastic lintels (compare with Fig. 7 b in section 3.1.2).

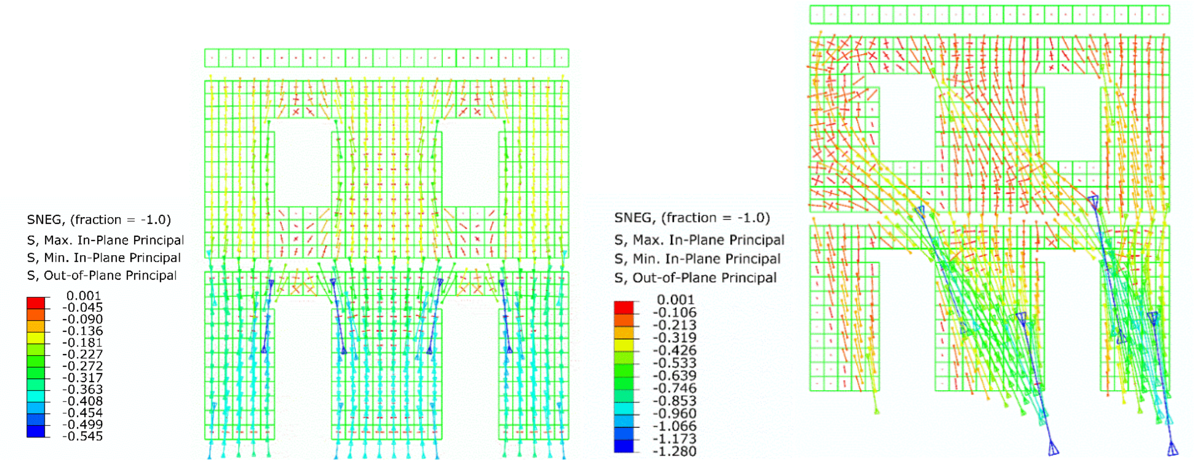

Fig. 11. "Pavia experiment", simulation of gravity load: Principal stresses in masonry: a) gravity load, b) horizontal load 100 kN.

The capacity curve up to the limit load is computed using the algorithm presented in section 2.4, by using an initial guess, $\Delta F = 50\ kN$ and a tolerance, $F_{tol} = 2kN$. The limit load is found to be 178kN, corresponding to reaching the compressive strength in the right pier.

The solutions obtained at two values of the lateral load *F* are reported in Fig. 13a, b. The first one corresponds to a lateral load of 100 kN. In these conditions the structure behaves nearly elastically. Slight cracks are noted in the ground piers due to heel tension and some others in the connecting spandrel of the first floor. The second value of *F* corresponds to the limit load, here estimated, 178 kN. It exceeds the experimental peak load by 18%, but this can be motivated considering that a monotonic numerical capacity curve is compared with the experimental envelope of the cyclic load-displacement diagram. At this load, the minimum (compressive) principal stress is about 3 MPa, corresponding to the reported strength in compression of masonry. The lateral load is supported nearly entirely by the central and the right pier, while at this stage the left pier is nearly completely damaged.

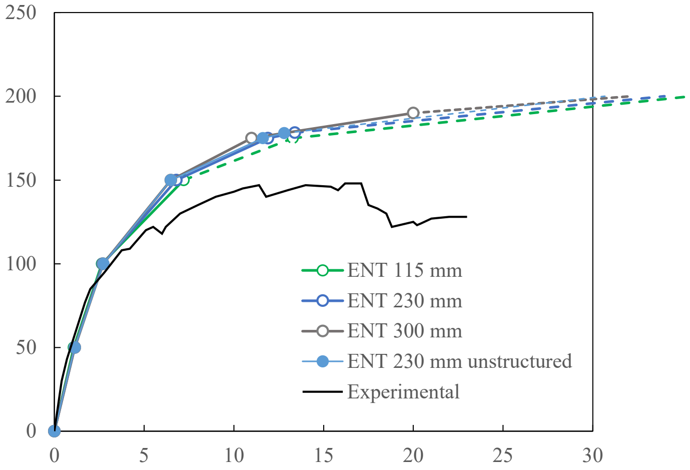

Fig. 12. Comparison of the numerical capacity curves obtained after mesh variations with the envelope of the experimental cyclic load-displacement curve (the dashed part of the curves correspond to violation of the compressive strength criterion).

Upon mesh variation the capacity curve based on the ENT material model remains nearly unchanged. The computed displacements are found to slightly increase up to 1% within 70% of the limit load, and up to 5% as the collapse load is approached. This has nearly no impact for practical applications. The most important difference is observed on the computed maximum principal compressive stress, which tends to increase at the corner regions upon mesh refinement. The compressive strength of 3 MPa is reached at 190 kN, 178 kN and 150 kN lateral load, depending on the mesh dimension (300 mm, 230 mm, 115 mm), Fig. 13.

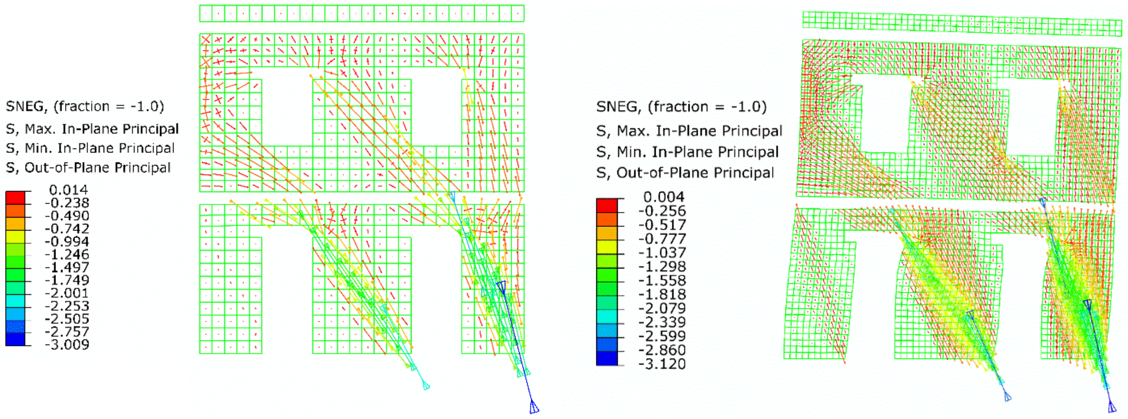

Fig. 13. Pavia building: principal stresses in the ENT material at a lateral load of: a) 178kN (230 mm mesh)), b) 150 kN (115 mm mesh).

3.2 Ground settlement analysis

3.2.1 2D wall affected by ground settlements

The aim is now to evaluate the ability of the ENT model to simulate the effects of ground settlements at the base of a masonry wall. Consider a wall 3.2 m long, 0.6 m deep and 0.1 m thick, resting over a strip foundation. Only the central part of the foundation, 1.2 m long, is affected by ground settlements (Fig. 14). The modulus of elasticity of masonry is assumed 1020 MPa. The panel is discretized with a mesh 75 x 75 mm^2. The wall is analyzed under gravity load, and ground settlements are simulated by removing any constraint at the nodes of the central region.

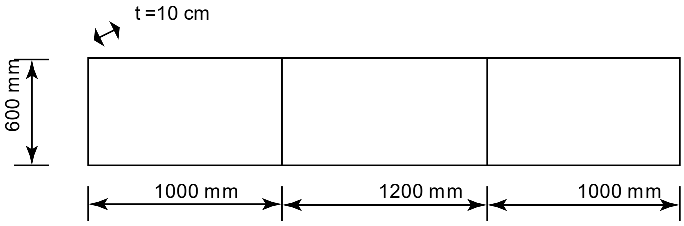

Fig. 14. Masonry wall scheme.

The numerical simulations show that a relieving arch occurs (Fig. 15), as commonly observed in unreinforced masonry structures. At the ends of the region experiencing settlements, higher inclined compressive stresses occur. In the rest of the model, which is unaffected by settlements, only vertical compressive stresses develop.

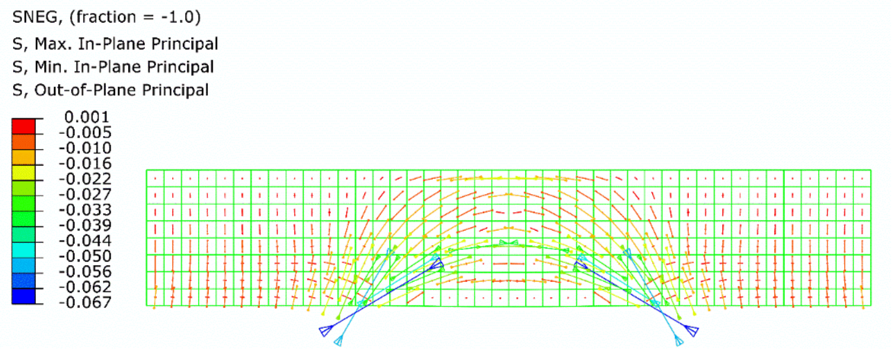

Fig. 15. Masonry wall experiencing ground settlements: principal stresses from the ENT simulation.

The formation of the arch-like compressive stress path has a marked effect on the distribution of the displacement field. In fact, compared to the elastic case (Fig. 16a), where settlement affect also the neighbouring regions, in an ENT wall displacement are localized beneath the internal arch (Fig. 16b). The zone above the arch experiences reduced displacements, while the rest of the model is virtually undeformed. This is in line with the schemes proposed by Mastrodicasa [31] regarding the effects of ground settlements in masonry walls (Fig. 16c).

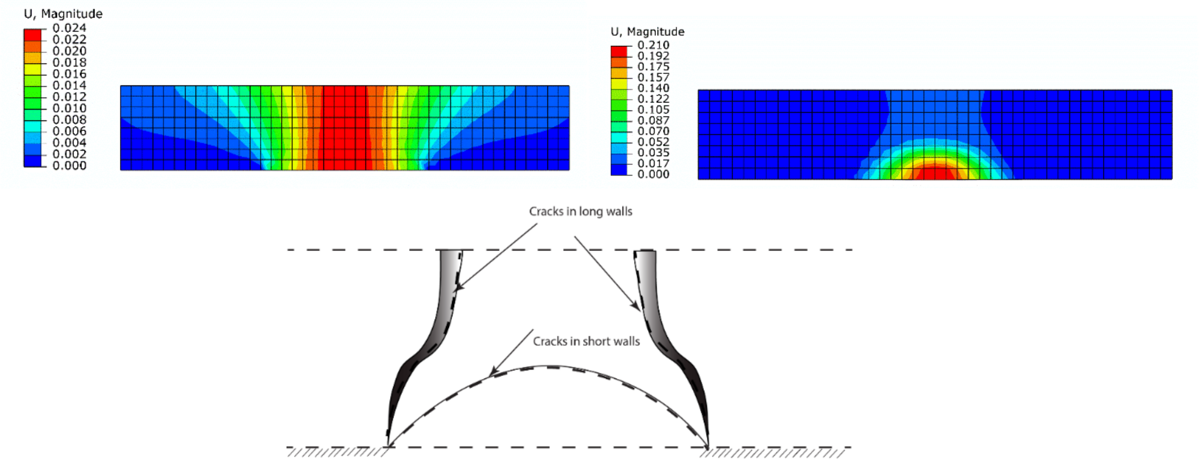

Fig. 16. Masonry wall experiencing ground settlements: contours of the displacement a) in the elastic model or b) in the ENT model; c) Schematic crack pattern after Mastrodicasa [31].

3.2.2 Intersecting walls experiencing ground settlements

This case is the 3D extension of the previous one. The geometry of the intersecting walls is created through a rotation of 90° of one of the walls about its symmetry axis (Fig. 14).

A small modification is carried out to the FE code by adopting shell elements. The structure of the code remains the same, the only change being that the damage values (or material densities) are computed at different section points along the shell thickness (5 points, in the application shown hereafter). Through these modifications, it is possible to obtain ENT solutions for plane structures in 3D configurations.

In the present example, the domain is discretised with 3D shell elements, labelled S4R in Abaqus Standard. Similarly to what observed in the 2D case, an arch-like stress flow (Fig. 17) is observed in both walls in the region affected by ground settlements (Fig. 18).

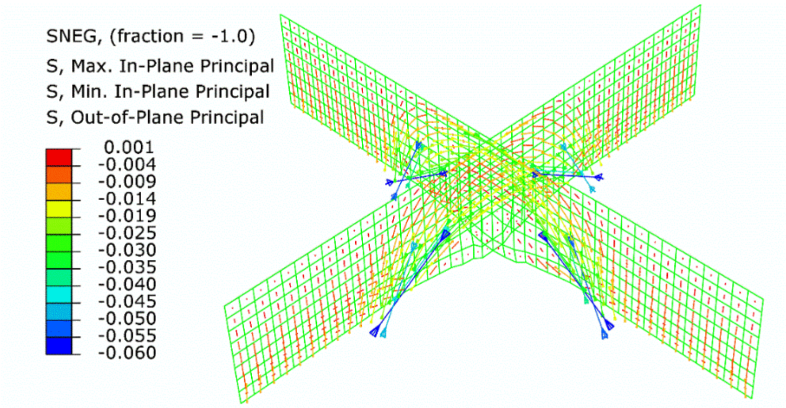

Fig. 17. Intersecting walls experiencing ground settlements: principal stresses.

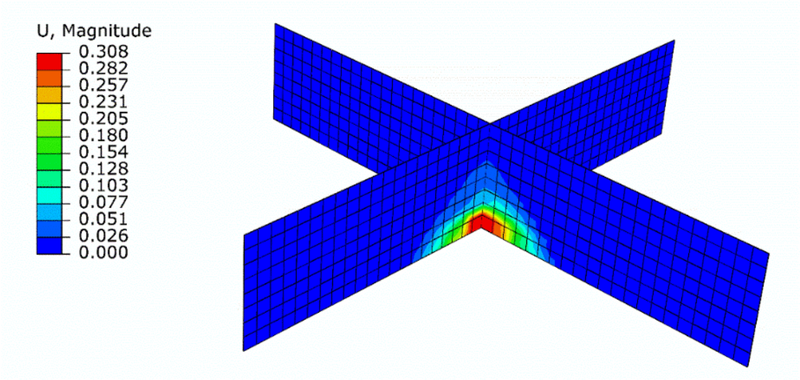

Fig. 18. Intersecting walls experiencing ground settlements: contours of the displacement.

3.2.3 Masonry façade experiencing ground settlements

The example of the Pavia case is here resumed, by assuming a hypothetical inelastic settlement over the central support. The aim is to test the formation of the internal arch mechanism which is typically observed in masonry structures. An inelastic settlement of 2 mm is prescribed at the central pier, while the boundary conditions remain fixed in the two other piers. A similar test was performed previously also in [16, 32]. Three types of structured mesh dimensions are tested, 300 mm, 230 mm, and 115 mm, in addition to a 230 mm unstructured mesh (Fig. 19).

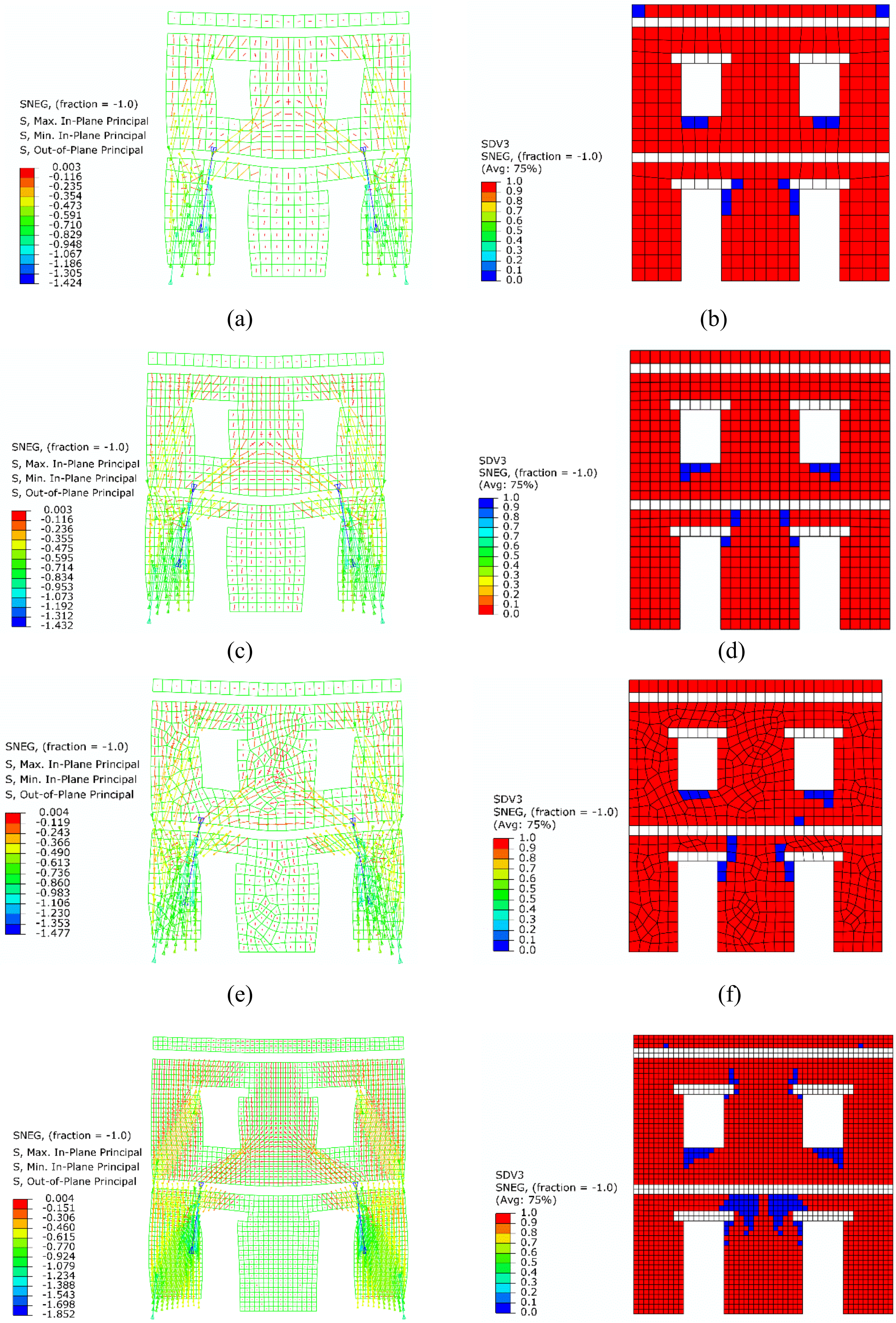

(a) (b)

(c) (d)

(e) (f)

(g) (h)

Fig. 19. Masonry façade with central settlement: left column – principal stresses; right column – void regions (elements in blue). a, b) mesh size 300 mm, c, d) mesh size 230 mm, e, f) mesh size 230 mm (unstructured), g, h) mesh size 115 mm.The numerical results show that the arch-like stress flow

deviates to increase the load in the solid masonry regions between the openings (Fig. 19). The void regions which can be related to the crack pattern are localized below the arch, as well as in the spandrels under the windows. Upon mesh refinement the observed settlement mechanism remains the same, with the formation of the internal arch and the internal load-redistribution. Differences are mostly related to the extension of the void regions (Fig. 19). In particular, in the unstructured mesh a slightly non symmetric distribution of damage can occur. This, however, could be kept under control by discretizing with elements of similar size or further mesh refinement. After the redistribution of the loads due to the settlements, the internal pier is mostly loaded by the weight of the first floor and by its self-weight. Accordingly, the maximum stress in the outer piers is nearly three times higher than that under self-weight only. In particular, higher values of stresses are noted at the corner regions when undergoing homothetic mesh refinement (Fig. 19c, e). Depending on the quality of masonry (compressive strength), this can become an important issue [33].

3.2.4 Experimental settlement-induced cracks in a scaled masonry façade

The experiment carried out by Giardina et al. [34, 35] on a 1/10th scaled masonry façade subjected to tunnel-induced settlement is adopted to test the ENT material model. The façade is 1428mm long, 1186mm deep and 50mm thick. The upper openings are 126mm wide, while the one in the ground are 336 mm wide (Fig. 20a). Wooden lintels support masonry atop the openings. The façade is supported by steel beam, 1700 mm long. The beam is fixed for 115mm, while roller supports have been placed at the left end of the base and below the right door (Fig. 20b). The point loads reported by Giardina in [34] are applied to simulate floor loads. The experimental crack pattern shows cracks distributed in part of the façade at the right side of the central support (Fig. 20). The left part of the façade is reported to move and rotate almost rigidly, with no major cracks appearing [34] (Fig. 20b).

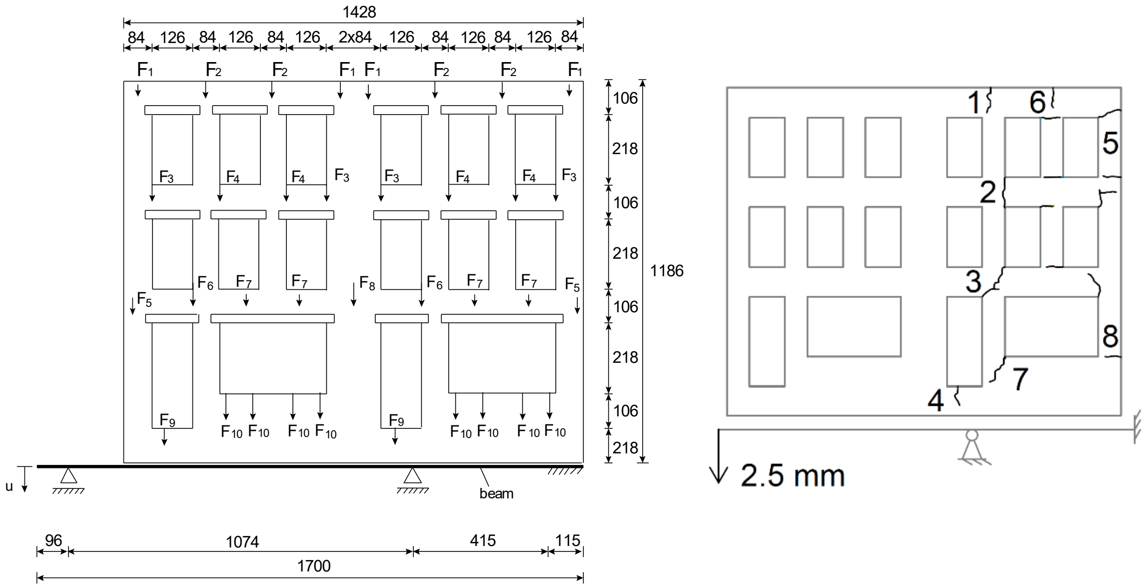

Fig. 20. Façade tested by Giardina et al. [34, 35]: a) Geometry of experimental setup [mm], b) Reported damage pattern at 2.5mm.

The numerical model developed in the present study has 3495 elements, with sides having a length between 17 and 20mm. Two element types are used: B31 for the beam and CPS4R for the wall, according to Abaqus' nomenclature. The present simulation assumes plane stress conditions; beam and plane stress elements are supposed to be tied.

The simulation results are reported in Fig. 21 The principal stresses show the presence of internal arches above the main openings (Fig. 21a). The crack pattern is relatively well matched by the void regions in the right part of the model (Fig. 21b), whereas in the left part the predicted cracks are more extended than in the experiment. Indeed, a no-tension material model is expected to predict more damage with respect to the cracks observed in masonry constructions, as the tensile strength is nonzero although small.

In terms of kinematics, there is a nearly perfect matching regarding the vertical displacement of the monitored point (Fig. 22a). In the horizontal direction, the agreement is good up to 5mm, whereas, as the load increases, the discrepancy between predicted and measured displacements becomes more significant (Fig. 22b).

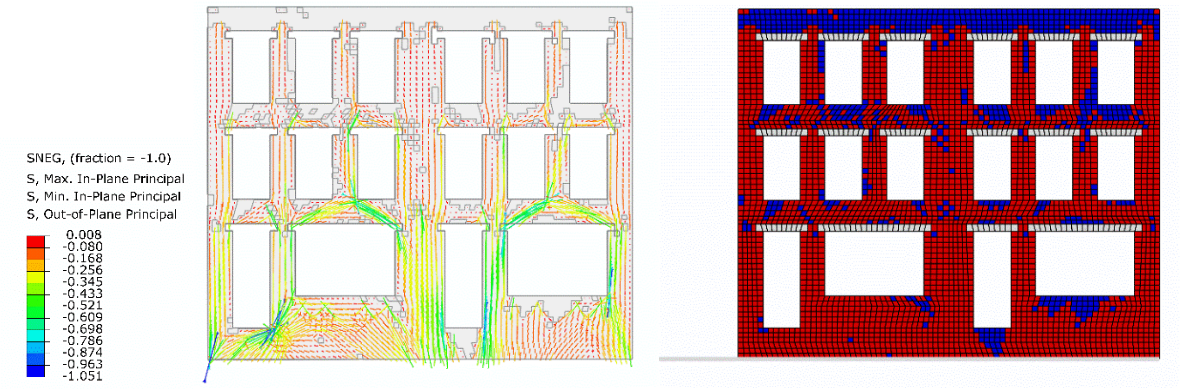

Fig. 21. Façade tested by Giardina et al. Simulation of a 2.5mm settlement: a) Principal stresses, b) Void regions (in blue).

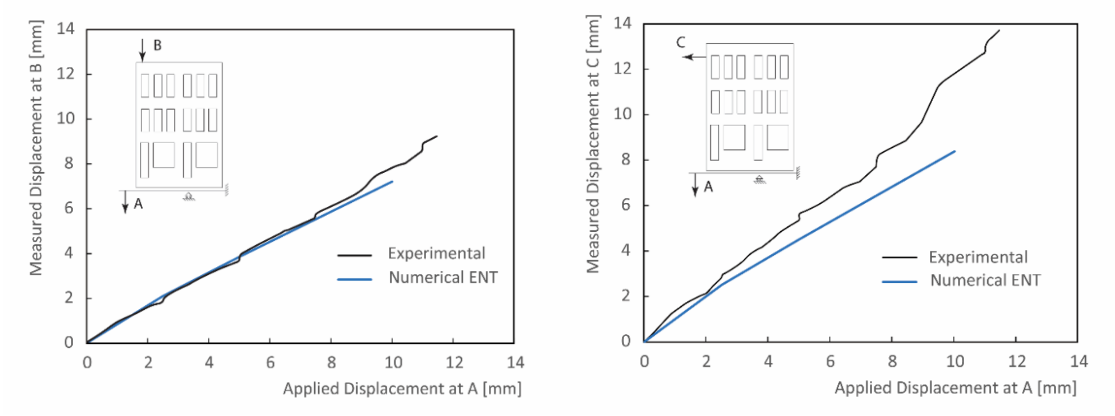

Fig. 22. Façade tested by Giardina et al.: a) Vertical displacement applied of point A vs vertical displacement at point B; (b) vertical displacement applied at point A vs horizontal displacement at point C.

4 Conclusions

The implementation of the Elastic No-Tension (ENT) material model within the framework of Sequential Linear Analysis has been presented. The proposed implementation aims at solving structural problems related to masonry structures. The limited number of parameters required by the ENT model makes it very appealing for the analysis of unreinforced masonry constructions compared to more refined mathematical models, since data and resources for experimentation are limited. The ENT model can predict collapse loads computed by means of Rigid No-Tension models with no a priori assumption on the kinematics. Also, it can be conveniently used to deal with ground settlements.

The implementation is developed through the combined application of a user subroutine in Abaqus, Python and Matlab scripts. In the SLA framework, a number of elastic analyses are launched sequentially. During this step-by-step process, the isotropic material is substituted with an orthotropic one, which exhibits negligible stiffness along the material axis (or axes) where a positive principal stress is found. The equivalent orthotropic material shares the same symmetry directions with the principal stresses. Convergence of this sequential process is achieved when the strain energy of the system finds a plateau.

A number of benchmark cases, considering dead and live vertical loads, lateral loads and ground settlements, have been analysed to assess the capabilities of the proposed model. In the case of lateral loads, the capacity curves match the experimental curves satisfactorily up to the collapse load. When dealing with horizontal loading, it has been shown that a finite strength in compression is necessary in order to account for the phenomenon of toe crushing. Furthermore, this can account for the prediction of limit displacements by interrupting the simulations when a given value of the compressive stress is found somewhere in the model. In the case of ground settlements, the distribution of cracking strains mostly agrees with the crack pattern at the onset of collapse, whereas in service conditions the simulation predicts cracking more severe than what experimentally observed. This is likely to be related to the assumption that the material has no tensile strength. The numerical predictions of the capacity curves were found to be quite unaffected by mesh refinement and layout, which confirms the inherent robustness of the proposed model. As expected, finer meshes can be conveniently adopted to increase the accuracy in the approximation of the stress field.

Based on the above observations, the proposed approach can be conveniently used to preliminary investigate the behaviour of masonry constructions, especially historical buildings with negligible tensile strength.

Future developments of the research will be focused on the implementation of the ENT model for 3D solids, as well as on a full coding through Fortran subroutines in Abaqus, to avoid the need for auxiliary scripts in order to speed up the simulations.

References

[1] Del Piero G. Constitutive equation and compatibility of the external loads for linear elastic masonry-like materials. Meccanica 1989;24:150-62.

[2] Heyman J. The stone skeleton. International Journal of solids and structures 1966;2:249-79. https://doi.org/10.1016/0020-7683(66)90018-7

[3] Di Pasquale S. Statica dei solidi murari: teoria ed esperienze: Dipartimento di costruzioni; 1984.

[4] Angelillo M, Fortunato A, Gesualdo A, Iannuzzo A, Zuccaro G. Rigid block models for masonry structures. International Journal of Masonry Research and Innovation 2018;3:349-68. https://doi.org/10.1504/IJMRI.2018.095701

[5] Iannuzzo A, Van Mele T, Block P. Piecewise rigid displacement (PRD) method: a limit analysis-based approach to detect mechanisms and internal forces through two dual energy criteria. Mechanics Research Communications 2020;107:103557. https://doi.org/10.1016/j.mechrescom.2020.103557

[6] Iannuzzo A, Dell'Endice A, Van Mele T, Block P. Numerical limit analysis-based modelling of masonry structures subjected to large displacements. Computers & Structures 2021;242:106372. https://doi.org/10.1016/j.compstruc.2020.106372

[7] Angelillo M, Lourenço PB, Milani G. Masonry behaviour and modelling. 2014;551:1-26. https://doi.org/10.1007/978-3-7091-1774-3_1

[8] Heyman J. The masonry arch. 1982.

[9] Pepe M, Sangirardi M, Reccia E, Pingaro M, Trovalusci P, De Felice G. Discrete and continuous approaches for the failure analysis of masonry structures subjected to settlements. Frontiers in Built Environment 2020;6:43. http://dx.doi.org/10.3389/fbuil.2020.00043

[10] Iannuzzo A, Angelillo M, De Chiara E, De Guglielmo F, De Serio F, Ribera F, et al. Modelling the cracks produced by settlements in masonry structures. Meccanica 2018;53:1857-73. https://doi.org/10.1007/s11012-017-0721-2

[11] Angelillo M. Constitutive relations for no-tension materials. Meccanica 1993;28:195-202.

[12] Lourenco PB. Computational strategies for masonry structures. Ph.D. Thesis. Delft University of Technology, Delft, The Netherlands; 1996.

[13] Roca P, Cervera M, Pelà L, Clemente R, Chiumenti M. Continuum FE models for the analysis of Mallorca Cathedral. Engineering Structures 2013;46:653-70. http://dx.doi.org/10.1016/j.engstruct.2012.08.005

[14] Cusano C, Angjeliu G, Montanino A, Zuccaro G, Cennamo C. Considerations about the static response of masonry domes: a comparison between limit analysis and finite element method. International Journal of Masonry Research and Innovation 2021;6:502-28. http://dx.doi.org/10.1504/ijmri.2021.118835

[15] Angelillo M. A finite element approach to the study of no-tension structures. Finite elements in analysis and design 1994;17:57-73.

[16] Angelillo M, Cardamone L, Fortunato A. A numerical model for masonry-like structures. Journal of Mechanics of Materials and Structures 2010;Volume 5, No. 4. http://dx.doi.org/10.2140/jomms.2010.5.583

[17] Bruggi M. Finite element analysis of no–tension structures as a topology optimization problem. Structural and Multidisciplinary Optimization 2014;50:957-73. http://dx.doi.org/10.1007/s00158-014-1093-z

[18] Bruggi M, Taliercio A. Analysis of no-tension structures under monotonic loading through an energy-based method. Computers & Structures 2015;159:14-25. http://dx.doi.org/10.1016/j.compstruc.2015.07.002

[19] Briccola D, Bruggi M. Analysis of 3D linear elastic masonry-like structures through the API of a finite element software. Advances in Engineering Software 2019;133:60-75. https://doi.org/10.1016/j.advengsoft.2019.04.009

[20] Pari M, Hendriks M, Rots JG. Non-proportional loading in sequentially linear solution procedures for quasi-brittle fracture: A comparison and perspective on the mechanism of stress redistribution. Engineering Fracture Mechanics 2020;230:106960. https://doi.org/10.1016/j.engfracmech.2020.106960

[21] Pari M, Hendriks MA, Rots JG. Non-proportional loading in sequentially linear analysis for 3D stress states. International Journal for Numerical Methods in Engineering 2019;119:506-31. https://doi.org/10.1002/nme.6060

[22] Bruggi M, Taliercio A, Cinquini C. Analysis of no-tension bodies through a topology optimization approach. XXI AIMETA 2013:1-10.

[23] Papa E, Taliercio A. A non-rotating anisotropic damage model for brittle materials. Proceedings of International center for numerical methods in engineering2005.

[24] Andreassen E, Clausen A, Schevenels M, Lazarov BS, Sigmund O. Efficient topology optimization in MATLAB using 88 lines of code. Structural and Multidisciplinary Optimization 2011;43:1-16. https://doi.org/10.1007/s00158-010-0594-7

[25] Yu C. From sequentially linear analysis to incremental sequentially linear analysis: Robust algorithms for solving the non-linear equations of structures of quasi-brittle materials. Ph.D. Thesis. Delft University of Technology, Delft, The Netherlands; 2019.

[26] Voormeeren L. Extension and verification of sequentially linear analysis to solid elements. Master Thesis. Delft University of Technology, Delft, The Netherlands; 2011.

[27] Rots JG, Blaauwendraad J. Crack models for concrete, discrete or smeared? Fixed, multi-directional or rotating? HERON, 34 (1), 1989 1989.

[28] Esposito R, Ravenshorst GJ. Quasi-static cyclic in-plane tests on masonry components 2016/2017. Master Thesis. Delft University of Technology, Delft, The Netherlands; 2017.

[29] Messali F, Esposito R, Jafari S, Ravenshorst G, Korswagen P, Rots JG. A multiscale experimental characterisation of Dutch unreinforced masonry buildings. 16th European conference on earthquake engineering, Thessaloniki 2018.

[30] Magenes G, Kingsley G, Calvi G. Seismic Testing of a Full-Scale, Two-Story Masonry Building: Test Procedure and Measured Experimental Response: University of Pavia; 1995.

[31] Mastrodicasa S. Dissesti statici delle strutture edilizie. Diagnosi e consolidamento. 1958.

[32] Iannuzzo A, Block P, Angelillo M, Gesualdo A. A continuous energy-based numerical approach to predict fracture mechanisms in masonry structures: CDF method. Computers & Structures 2021;257:106645. https://doi.org/10.1016/j.compstruc.2021.106645

[33] Binda L. Learning from failure: long-term behaviour of heavy masonry structures: WIT press; 2008.

[34] Giardina G, Marini A, Hendriks MAN, Rots JG, Rizzardini F, Giuriani E. Experimental analysis of a masonry façade subject to tunnelling-induced settlement. Engineering Structures 2012;45:421-34. https://doi.org/10.1016/j.engstruct.2012.06.042

[35] Giardina G. Modelling of settlement induced building damage. PhD Thesis. Delft University of Technology, Delft, The Netherlands; 2013.